



## RESEARCH ARTICLE

10.1029/2019JC015301

## Phase-Coherent Amplification of Ocean Swells Over Submarine Canyons

## Key Points:

- The coasts of Toyama Bay in Japan have been devastated by severe swell events called YoriMawari-nami
- We characterize these events with data, ray tracing, and phase-averaged and phase-resolving models
- Phase-coherent amplification emerged as the key mechanism for matching observations

## Supporting Information:

- Supporting Information S1
- Movie S1

## Correspondence to:

H. Tamura,  
htamura@p.mpat.go.jp

## Citation:

Tamura, H., Kawaguchi, K., & Fujiki, T. (2020). Phase-coherent amplification of ocean swells over submarine canyons. *Journal of Geophysical Research: Oceans*, 125, e2019JC015301. <https://doi.org/10.1029/2019JC015301>

Received 17 MAY 2019

Accepted 20 JAN 2020

Accepted article online 27 JAN 2020

Hitoshi Tamura<sup>1</sup> , Koji Kawaguchi<sup>1</sup>, and Takashi Fujiki<sup>1</sup><sup>1</sup>Port and Airport Research Institute, Yokosuka, Japan

**Abstract** Ocean swells can be a significant coastal hazard, potentially causing coastal disasters with costly damage to infrastructure and tragic loss of lives. We have observed this in the coastal region of Toyama Bay in the Sea of Japan, which has been devastated by severe winter swell events (the so-called YoriMawari-nami; YM wave). An extreme swell event was recorded in February 2008 in which the wave height at a site in the bay reached 9+ m, which corresponds to 16 times the local climatological average. Substantial efforts by the Japanese coastal engineering community have been expended to reproduce YM wave events with phase-averaged wave models but, to our knowledge, with no success. During an archetype YM event, we found that the Noto peninsula filtered the incoming wavefield such that in the bay incident waves were quasi-monochromatic. The swell then refracted over a submarine canyon resulting in a bimodal directional distribution of wave energy. This initiated conditions favorable for coherent interference, violating the assumptions of the phase-averaged approach. Coherent interference is the key mechanism for understanding the formation of the large amplitudes and for matching observed high space-time variability. Our results demonstrate the significance of the coherent interference for wave statistics over coastal bathymetry; only by accounting for phase-resolving phenomena were we able to adequately reproduce the observations.

**Plain Language Summary** Waves, which originate in strong storms in the north of the Sea of Japan, have recently devastated the coastal region of Toyama Bay. These type of events have been known for centuries, and the locals refer to them as YoriMawari-nami. Engineers have struggled to understand the origin of YoriMawari-nami events, though important for protecting our coasts, and they have been unable to reproduce them with typical models (phase-averaged wave models). We used data to characterize these events, which are always long, old waves (swells) with unusually large wave heights compared to the past wave climate. We use wave models and ray-tracing techniques to show how a swell arrives in the bay and bends over submarine canyons. The submarine canyon, like a prism separating light into different colors, separates out swells, and wave phases (the exact timing of an individual wave cycle) can no longer be ignored. In fact, the wave phases become crucial for understanding the enhancement of wave height. We were able to reproduce the observations with a phase-resolving model, giving hope for predicting these events in the future.

## 1. Introduction

Wind-generated waves that propagate on the ocean surface can be roughly categorized into wind seas or swells based on whether or not waves are actively receiving energy from wind. Generally, swells are long, fast (i.e., faster than the local wind speed) waves that formed in distant weather systems. Ocean swells play a number of related roles in coastal dynamics. Swells generate the nearshore currents that control beach erosion. Swells can be a significant coastal hazard, potentially initiating coastal disasters with costly damage to infrastructure and tragic loss of lives.

Swells are generated from the spectral downshifting of wind seas by resonant interactions where wave energy is transferred from the shorter to longer waves (e.g., Badulin & Zakharov, 2017; Hasselmann et al., 1973; Kats & Kontorovich, 1971; Young & Van Vledder, 1993; Zakharov, 2018; Zakharov et al., 2019). Swells can travel great distances with little attenuation, propagating to coasts far from where they were generated (e.g., Ardhuin et al., 2009; Munk et al., 1963; Snodgrass et al., 1966). As a swell propagates from deep to shallow water, the spatial distribution of swell energy begins to vary more strongly and on smaller scales

©2020. The Authors.

This is an open access article under the terms of the Creative Commons Attribution License, which permits use, distribution and reproduction in any medium, provided the original work is properly cited.

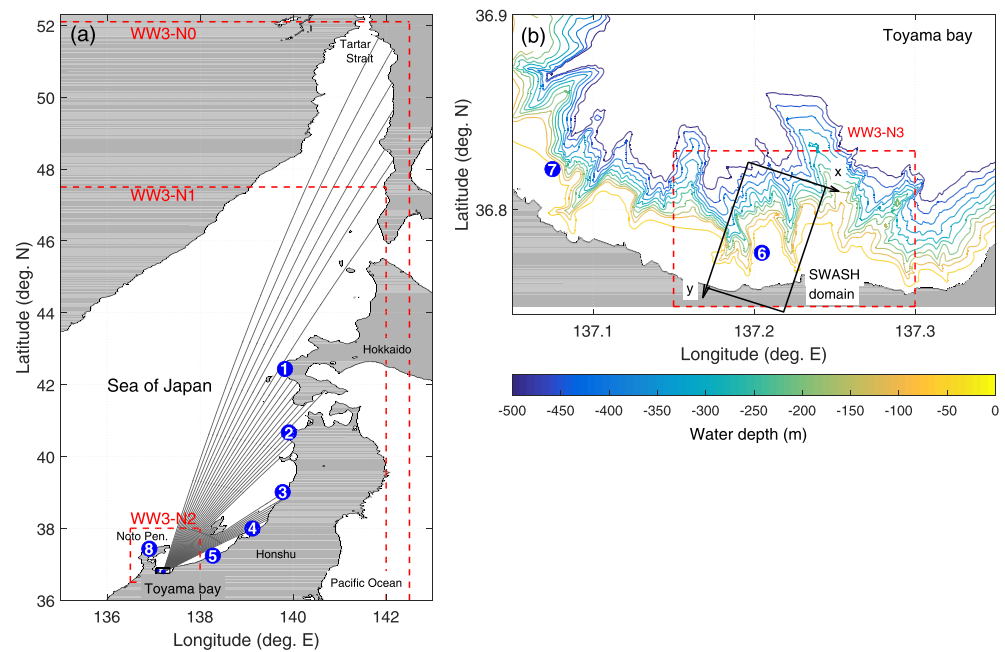


**Figure 1.** (a) Map of the Sea of Japan and Toyama bay with NOWPHAS observational sites (blue dots with numbers) listed in Table 1. Red dashed boxes mark the computational domains of WW3-N0, WW3-N1, and WW3-N2. Solid lines represent the backward ray tracing for all directions arriving at Toyama site (#6). (b) An enlarged view near the southern margin of the Toyama bay (black rectangle in (a)). Red dashed and black boxes indicate the computational domains for WW3-N3 and SWASH models, respectively. Shallow water bathymetry (0–500 m) of M7000 database is shown by color contours.

dictated by interaction with the local bathymetry through the refraction, diffraction, interference, shoaling, and bottom-induced breaking (e.g., Cavaleri et al., 2007; Didenkulova et al., 2009; Magne et al., 2007).

In this paper, we address the process of swell transformation near the coast and the formation of dangerous wave events. The region of interest is the coastal region of the Toyama Bay (TB) in the Sea of Japan (Figure 1). This region has been devastated by severe winter swell events. Dating back to the Edo period in the eighteenth century, these events have been known to local people who refer to them YoriMawari-nami (hereafter referred to as YM wave events) that roughly translates to approaching and turning waves. Low-pressure systems (i.e., polar lows) (e.g., Tsuboki & Wakahama, 1992; Yanase et al., 2016) can develop rapidly over the northern part of the sea (40–45°N) moving eastward but then stall off the east coast of Hokkaido. This sets up a northeasterly wind that blows along the west coast of Hokkaido over a long fetch. YM wave events tend to appear as these lows propagate out over the Sea of Japan and the local weather calms. Evidently, as will be shown, wave rays for all directions arriving in the TB go through the west coast of Hokkaido and originate from the Tartar Strait (Figure 1a).

The TB is a semienclosed bay approximately 30 km wide and 25 km long covering an area of 750 km<sup>2</sup>. The bay is partially exposed to the Sea of Japan on the east side and sheltered on the north and west sides by the Noto Peninsula (Figure 1a). Due to the geometry of the coastline, wind seas generated by seasonal northwesterly wind are blocked, so high sea states are typically due to swells entering the bay from the NNE. In the southern margins of the bay where YM wave events have been observed, there is a narrow continental shelf (around 4 km wide) with distinct submarine canyons (Figure 1 b). An extreme swell event was recorded in February 2008 (e.g., Kohno et al., 2009) in which wave height at a site (site #6 in Figure 1b) reached 9+ m, which corresponds to 16 times the local climatological average. This event caused unfortunate casualties and tremendous damage to infrastructure. The societal concern over coastal disasters like this, combined with the unique nature YM wave events, has catapulted this issue to the forefront of the list of challenges facing wave researchers and coastal engineers in Japan.

Substantial efforts by the Japanese coastal engineering community have been expended to reproduce YM wave events with phase-averaged wave models (e.g., Ohta et al., 2016) but, to our knowledge, with no

success. One point that perhaps has yet to be appreciated is that some features of YM wave events may be a result of phase-coherent wave dynamics. There have been a few studies demonstrating the significance of the coherent interference for wave statistics over coastal bathymetry. A series of studies by Smit and Janssen (2013) and Smit et al. (2016) have demonstrated that the smaller-scale variability of observed wave height can be well explained by the effect of coherent interference over submarine canyons off the La Jolla, CA, USA, and the San Francisco bar at Ocean Beach, CA, USA. We show here that a coherent wavefield is generated over the continental shelf, and coherent interference is the missing piece of the puzzle for understanding the modulation of local wave statistics and the formation of the large-amplitude waves.

The theoretical framework of coherent wave interference in the coastal regions was also established by Smit and Janssen (2013) and Smit et al. (2015). Generally, a wavefield can be represented by  $N$  components of plane waves in space,  $\mathbf{x}$ , and time,  $t$ . Then the surface elevation  $\eta_n(\mathbf{x}, t) = \text{Re}(\zeta_n(\mathbf{x}, t))$  where  $\zeta_n = A_n e^{i\phi_n}$  ( $n = 1, \dots, N$ ),  $\phi_n = \mathbf{k}_n \cdot \mathbf{x} - \omega(\mathbf{k}_n)t$  is wave phase, and  $A_n$ ,  $\mathbf{k}_n$ , and  $\omega(\mathbf{k}_n)$  are wave amplitude, wavenumber vector, and angular frequency. The angular frequencies are related to the wavenumber by the linear dispersion relation  $\omega(\mathbf{k}_n) = \sqrt{gk \tanh k_n h}$ , where  $k_n = |\mathbf{k}_n|$  and  $h$  is the mean water depth. Then, the intensity (or wave envelope squared),  $I$ , of their linear superposition in physical space can be derived as

$$I(\mathbf{x}, t) = \sum_{n=1}^N \sum_{m=1}^N \zeta_n \zeta_m^* = \sum_{n=1}^N \zeta_n \zeta_n^* + \sum_{n=1}^N \sum_{m \neq n}^N \zeta_n \zeta_m^* \quad (1)$$

$$= \sum_{n=1}^N A_n^2 + 2 \sum_{n=1}^N \sum_{m > n}^N A_n A_m \cos(\Delta \mathbf{k}_{nm} \cdot \mathbf{x} - \Delta \omega_{nm} t)$$

where the asterisk notation \* indicates the complex conjugate,  $\Delta \mathbf{k}_{nm} = \mathbf{k}_n - \mathbf{k}_m$ , and  $\Delta \omega_{nm} = \omega(\mathbf{k}_n) - \omega(\mathbf{k}_m)$ . In equation (1), the first term in the right-hand side represents the contribution from autocorrelation function corresponds to the variance spectrum. The variance spectrum is the prognostic variable in phase-averaged models. The second term, with phase information, represents the cross-correlation function between noncollinear wave modes and represents wave interference. When a number of wave components are superimposed with random phases, the phase-coupled process is averaged out (i.e., incoherent interference), which is the fundamental assumption underlying phase-averaged models (e.g., Smit & Janssen, 2013; Tolman, 2009). Crucially, this assumption may not hold for YM wave events as we will later show.

The purpose of this study is to investigate the characteristics of the YM wave events in the TB, particularly regarding the generation mechanism of very large swells over the continental shelf and submarine canyons. We utilize a suite of tools: analysis of wave observations in TB and the surrounding region in the Sea of Japan; hindcasts and sensitivity studies with phase-averaged and phase-resolving models; and analytical ray tracing exercises. Combining these tools allows us to better understand the underlying wave dynamics and explore the potential predictability of YM wave events. The remainder of the paper is organized as follows. Section 2 describes the in situ data sets and model configurations. In section 3, we show observations and hindcasts of a particular YM wave event. We then investigate the YM waves based on a phase-resolving model. We discuss the formation of YM waves in the context of coherent interference in section 4. Conclusions are provided in section 5.

## 2. Data and Methods

### 2.1. Wave Observations and Detection of the YM Wave Events

Wave data in this study come from the NOWPHAS (Nationwide Ocean Wave information network for Ports and HarbourS) observational network, which has been developed and maintained by the Ministry of Land, Infrastructure, Transport and Tourism in Japan since the 1970s. We mainly focus on data from 2007 to 2016 at the Toyama site (#6), but also examine seven other sites along the northeastern coast of the Sea of Japan (Table 1 and blue dots with numbers in Figure 1). The most obvious difference between observational sites inside and outside of the TB is coastal geometry and bottom topography. Toyama (#6) and Fushiki (#7) in the TB are located over the continental shelf with submarine canyons (Figure 1b), whereas other sites in the Sea of Japan are directly exposed to the wind and waves over a nearly flat bottom.

Time series of sea surface elevations were measured by bottom-mounted ultrasonic wave gauges (Sonic Corporation USW-1000) with a 2-Hz sampling rate and 20-min analysis windows. The electrical signal error of USW-1000 devices is less than 1% against the maximum output voltage. Quality control procedures were applied on raw data and unrealistic signals were filtered out before spectral analysis. One-dimensional

**Table 1**  
The Location #, Names, Positions, and Water Depth for NOWPHAS Observation Sites

Location #	Name	Latitude (°N)	Longitude (°E)	Depth (m)
1	Setana	42.4442	139.8175	52.9
2	Fukaura	40.6594	139.9117	51.0
3	Sakata	39.0086	139.7792	45.9
4	Niigata	38.0047	139.1261	34.5
5	Naoetsu	37.2358	138.2736	32.7
6	Toyama	36.7778	137.2050	20.0
7	Fushiki	36.8208	137.0747	46.4
8	Wajima	37.4308	136.9022	52.0

frequency wave spectra,  $F(f)$ , were estimated using the fast Fourier transform up to the 1-Hz Nyquist frequency, and a high-frequency cutoff was set to 0.75 Hz to exclude noise. We computed the usual statistical parameters such as the significant wave height ( $H_s$ ) and peak wave frequency ( $f_p$ ) from the wave spectra.

Because a swell may coexist with local wind sea (i.e., mixed sea state), it is necessary to define the swell components of wave energy within each spectrum. This ensures a consistent method for extracting YM wave events from historical records. Wind seas and swells were defined by a separation frequency  $f_c$  using a wave age criterion following Donelan et al. (1985) and Young (2006).

$$f_c = \frac{g}{2\pi \cdot 1.2u_{10}} \quad (2)$$

where  $g$  is the acceleration due to gravity and  $u_{10}$  is the mean wind speed at 10 m height. Because  $u_{10}$  is not available through the NOWPHAS, we utilize the Japan Meteorological Agency (JMA) Mesoscale Model (MSM) products for surface wind data (we use the same for forcing the wave hindcasts as will be explained later). We then calculate swell energy  $m_s$  and swell index  $SI$  defined as a fraction of swell energy in the total wave energy  $m_0$ :

$$m_s = \int_0^{f_c} F(f)df, \quad (3)$$

$$SI = \frac{m_s}{m_0} \in [0, 1] \quad (4)$$

The  $SI$  is used throughout the analysis to indicate swell-dominated wavefield.

## 2.2. Wave Modeling

### 2.2.1. Wave Hindcasts With WAVEWATCHIII

In order to investigate the YM wave events in the TB, wave hindcasts were conducted with a nested set up of the third-generation, phase-averaged wave model WAVEWATCHIII version 3.14 (WW3) (Tolman, 2009). For all calculations, we used the same parameterization schemes for the three main source terms. For the wind input and wave dissipation, the source term package by Bidlot et al. (2007) (ST3 switch) was used. We employed the discrete interaction approximation method (Hasselmann et al., 1985) for the non-linear interaction term. The shallow water source terms of bottom friction (Hasselmann et al., 1973) and the depth-induced breaking (Battjes & Janssen, 1978) were included for the innermost domain as will be described below. The ULTIMATE QUICKEST scheme with averaging was used for spatial and spectral propagation (Tolman, 2009). For all these, the default settings were used.

A one-way nesting approach was applied to efficiently focus on the TB in the Sea of Japan and to properly treat lateral boundary condition for the inner domain. We used a set of four nested grids referred to as WW3-N0, WW3-N1, WW3-N2, and WW3-N3 with  $1/5^\circ$  ( $\approx 20$  km),  $1/16^\circ$  ( $\approx 6$  km),  $1/80^\circ$  ( $\approx 1.2$  km), and  $1/1200^\circ$  ( $\approx 80$  m) resolutions (Figure 1), respectively. The outermost domain (WW3-N0) includes the whole ocean basin of the Sea of Japan and covers all potential source regions of YM wave events (as in Figure 1a). The WW3-N1 and WW3-N2 models were designed to capture generation and propagation of swells from the source region to TB. Finally, to resolve spatial distribution of coastal waves over the very narrow continental

**Table 2**  
*Computational Configurations for WW3 Model Hindcasts*

	WW3-N0	WW3-N1	WW3-N2	WW3-N3
Model domain	127.5–142.5°E 32.5–52.1°N	127.5–142.0°E 32.5–47.5°N	136.5–138.0°E 36.5–38.0°N	137.15–137.3°E 36.75–36.83°N
Spatial resolution	1/5° (~20 km)	1/16° (~6 km)	1/80° (~1.2 km)	1/1,200° (~80 m)
Frequency resolution	0.035–0.704 Hz (40 grids)			
Directional resolution	10° (36 grids)	2° (180 grids)	2° (180 grids)	1° (360 grids)
Surface wind	JMA/GSM	JMA/MSM	JMA/MSM	JMA/MSM
Open boundary	—	WW3-N0 (hourly)	WW3-N1 (30 min)	WW3-N2 (30 min)
Bathymetry	ETOPO1	JTOPO30v2	JTOPO30v2	M7000

shelves, we set up the innermost domain (WW3-N3) with a horizontal resolution of the order 80 m. The estimated wave spectra in the outer grids successively provided the lateral boundaries to the inner grids.

For all grids, the frequency domain was set to 40 bins logarithmically spaced from 0.035 to 0.704 Hz (relative frequency of 8%). This quantity of the increment parameter (1.08) was sufficient to resolve the narrow swell spectra in the frequency domain. A swell is also characterized by narrow directional spreading, so it was essential to progressively increase the directional resolution to accurately capture its propagation. The directional resolution for WW3-N1 and WW3-N2 was set to 2° (180 grids), and for WW3-N3 was set to 1° (360 grids).

The wave model was driven by the surface wind fields estimated by JMA operational atmospheric products (Global Spectral Model GSM: 6-hourly global fields with  $1/2^\circ \times 1/2^\circ$  resolutions, MSM: 3-hourly with  $1/20^\circ \times 1/16^\circ$  resolutions), and water depths were obtained from three bathymetry databases (ETOPO1, JTOPO30v2, and M7000) for each domain according to their regional coverages and resolutions. The computational configurations for all nests are summarized in Table 2.

### 2.2.2. Numerical Experiments with SWASH

To our knowledge, no prior work has identified wave interference and the associated phase-coherent amplification as the key mechanism for producing the YM wave events. Given this situation, it is possible that stochastic (i.e., phase-averaged) models are missing dynamic processes that are keys for reproducing these events. To test this possibility, we performed numerical experiments with the deterministic (i.e., phase-resolving) model Simulating WAVes till SHore (SWASH) (Zijlema et al., 2011). SWASH is a nonhydrostatic model based on the nonlinear, shallow water equations and has been widely validated and applied to investigate the nearshore wave processes in the field and in the laboratory (e.g., Smit et al., 2014; Suzuki et al., 2017).

SWASH was configured and driven by results from WW3. The coordinate system of SWASH was rotated into the mean incident swell direction (18° clockwise from north as seen in Figure 1b), which was calculated from the WW3-N2 hindcast. The offshore boundary condition was prescribed by the two-dimensional (2-D) wave spectra from WW3-N2. First, we randomly assign phase for the different wave components of 2-D spectra. These components drive sea surface elevation and orbital velocities along the offshore boundary. As for the lateral (open) boundaries, sponge layers with 500 m width are placed to avoid the wave reflection. A detailed description of the SWASH system can be found in Zijlema et al. (2011).

Model domain for SWASH ( $7.5 \times 4.5$  km) encompasses a part of the southern margins of TB (Figure 1b) where a NOWPHAS observation site (Toyama site #6) is centrally located. The horizontal resolutions were set to 10 m for down-wave ( $y$ ) direction and 15 m for cross-wave ( $x$ ) direction, consisting  $751 \times 301$  horizontal grid points. With an adequate number of vertical layers, SWASH can represent the nonhydrostatic pressure field which is crucial for dispersive wave propagation. The dispersion property of water waves is determined by dimensionless depth ( $kh$ ), and its maximum value of  $kh$  was roughly 8 in the domain. According to Zijlema et al. (2011), three vertical layers were adequate for accurately representing the linear wave dispersion for primary wave evolution in the model.

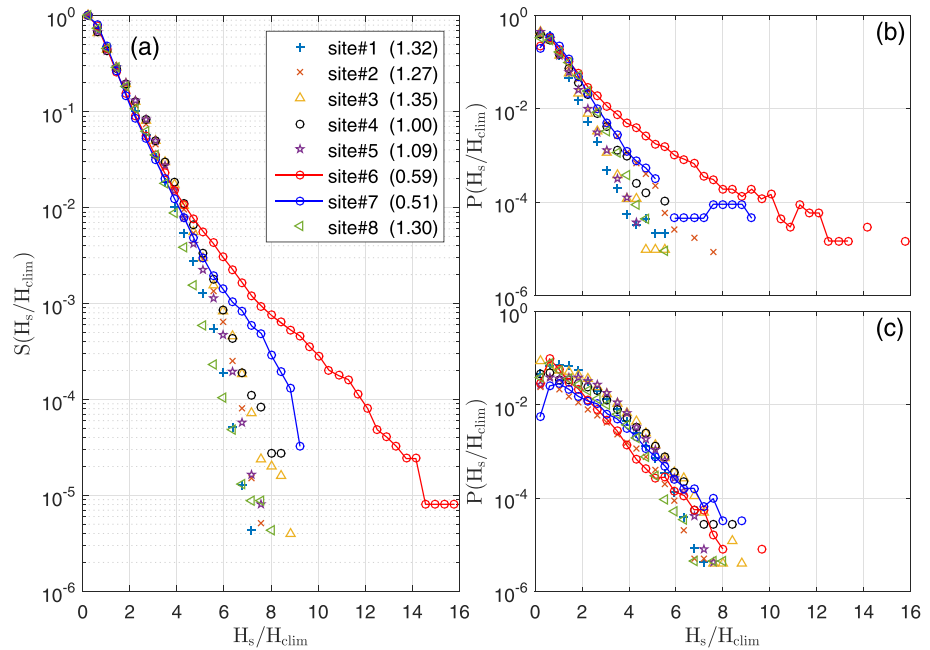


**Figure 2.** (a) Probability of exceedance of  $H_s$  at observational sites displayed in legend. The number in the legend represents the climatological average of  $H_s$  from 2007 to 2016:  $H_{s, clim}$  (m). (b) Probability distribution functions of  $H_s$  selected from historical data as swell-dominant condition ( $SI > 0.9$ ). (c) same as (b) but for wind sea and/or mixed conditions ( $SI < 0.5$ ).

The total duration of the SWASH computation was 30 min for each run which was initialized with zero state at each grid point. It takes a swell (with a period of 14 s) less than 10 min to transverse the model domain, so results were analyzed using the last 20 min of model runs. In total, 48 SWASH computations were carried out to cover the 2-day YM wave event.

### 3. Results

#### 3.1. Characterizing YM Wave Events from Observations

In order to characterize the unique features of YM wave events in the TB, we analyzed wave observations from 2007 to 2016 at eight sites along the coast of the Sea of Japan. The probability of exceedance of  $H_s$  for each site are shown in Figure 2a, representing a fraction of  $H_s$  exceeding  $x$  times larger than the local climatological mean of  $H_s$  (10-year average),  $H_{s, clim}$ . All profiles tend to fall into a single curve when  $H_s/H_{s, clim}$  is less than 4. However, the probability of exceedance for high waves (say,  $H_s/H_{s, clim} > 7$ ) in the TB is around 10 times larger than those outside of the bay. The tails are long, extending up to 16 and 9 at Toyama site (#6) and Fushiki site (#7), respectively. Figure 2b (Figure 2c) shows probability distribution functions (PDFs) of  $H_s$  selected from historical data with  $SI$  larger than 0.9 (smaller than 0.5) for swell (mixed and/or wind seas) dominated conditions. The PDFs of  $H_s$  for all locations indicate a similar pattern for wind and/or mixed sea conditions (Figure 2c). For swell-dominant conditions (Figure 2b), the PDFs of large  $H_s$  is higher and longer tails appear, again, at sites #6 and #7. This shows that higher than average wave conditions are typically swell dominated.

We define YM wave events by the following criteria: (1) swell-dominated ( $SI > 0.9$ ) and (2) large height relative to climatology ( $H_s/H_{s, clim} > 5$ ). Using these criteria at Toyama, a total of 26 events were found and are listed in Table 3. Time series of  $H_s$  corresponding to each event are given in Figure S1 in the supporting information. YM wave events typically appeared between October and April and twice a year on average. The duration of each event was a few days, and the mean wind speed, wave height, and wave period were in the range of 3–6 m/s, 1.5–4.5 m, and 10–14 s, respectively. The mean of peak wave direction fluctuates between around  $\pm 15^\circ$  from north. An interesting aspect of YM wave events was substantial variability in the time series of  $H_s$  over the event duration. The maximum  $H_s$  can easily reach twice the mean  $H_s$ , and scatter index of  $H_s$  (defined as a root mean squared value of  $H_s$  normalized by the mean values) can be

**Table 3**  
The YM Wave Events at Toyama Detected From Historical Data From 2007 to 2016

Case #	Starting time/date (JST)	Periods (hr)	Mean $u_{10}$ (m/s)	Mean $H_s$ (m)	Maximum $H_s$ (m)	Mean $T_p$ (s)	Maximum $T_p$ (s)	Mean direction	Scatter Index of $H_s$
01	00:00/08-Jan-2007	36.0	5.6	2.8	4.7	13.5	15.6	N/A	0.31
02	23:00/24-Jan-2008	23.0	5.7	2.6	3.9	12.5	13.9	-14.5	0.22
03	02:00/24-Feb-2008	38.0	5.5	4.5	9.4	12.9	16.7	1.9	0.49
04	14:00/09-Nov-2008	28.0	3.2	2.4	3.9	13.8	14.7	-3.9	0.26
05	08:00/02-Jan-2010	35.0	4.8	2.6	5.1	13.4	15.6	-4.5	0.32
06	14:00/13-Jan-2010	11.0	6.5	2.8	4.1	11.3	12.6	4.7	0.27
07	09:00/17-Jan-2011	21.0	5.9	2.4	3.4	12.2	13.9	-0.7	0.21
08	02:00/18-Apr-2011	29.0	4.6	2.1	3.5	12.6	13.9	5.6	0.20
09	17:00/26-Dec-2011	28.0	4.6	2.5	4.0	13.5	14.7	4.0	0.26
10	23:20/02-Nov-2012	20.7	3.6	2.3	3.5	11.4	13.2	3.7	0.21
11	23:20/04-Nov-2012	21.7	3.2	2.6	4.4	12.3	13.9	9.5	0.28
12	01:20/10-Nov-2012	36.0	3.8	2.5	4.4	11.2	13.2	7.6	0.27
13	22:20/15-Nov-2012	22.0	2.9	1.8	3.5	10.2	12.0	13.2	0.31
14	08:00/27-Jan-2013	26.0	3.2	2.0	3.9	13.2	15.6	-12.8	0.30
15	17:00/08-Feb-2013	34.0	3.6	1.8	3.5	12.4	15.6	-15.0	0.41
16	20:00/02-Mar-2013	42.3	3.3	2.8	5.0	13.5	16.7	-6.1	0.36
17	04:20/08-Apr-2013	27.7	4.9	2.1	3.4	12.8	14.7	-12.4	0.23
18	13:40/18-Dec-2014	28.7	4.2	3.9	8.4	13.4	16.7	8.7	0.43
19	07:40/08-Jan-2015	20.7	4.9	2.6	4.4	13.9	16.7	9.2	0.26
20	04:40/28-Feb-2015	24.3	3.6	2.4	4.5	12.5	15.6	-6.4	0.41
21	00:00/25-Mar-2015	36.3	3.1	2.2	3.7	11.6	14.7	12.4	0.36
22	07:00/09-Oct-2015	48.7	3.8	1.7	4.6	12.2	14.7	-2.8	0.46
23	00:00/26-Oct-2015	31.3	3.8	1.9	4.1	11.9	14.7	-2.5	0.42
24	17:40/20-Jan-2016	17.3	4.2	2.5	3.8	12.4	14.7	-3.0	0.22
25	10:40/01-Mar-2016	30.3	5.0	3.1	6.0	12.9	15.6	-0.8	0.44
26	18:00/23-Dec-2016	37.3	4.6	3.5	7.2	12.3	15.6	-2.2	0.44

more than 40% (Table 3). The temporal variations of  $H_s$  is a consistent feature across all YM wave events as demonstrated Figure S1.

In the following analysis, we investigate an archetype YM wave event, case 16. High variability of  $H_s$  was clearly observed during the event and could be an important signature of YM wave events. Meteorological and wave conditions are shown in Figure 3. Around 2 days before the event (Year Day 2013: 60.2–61), local wind speed (Figure 3a) exceeded 10 m/s and prevailing wind direction was NW (not shown).  $H_s$  (Figure 3b) did not correlate well with wind speed because of the fetch limited conditions. During this time, observed values of  $f_p$  were around 0.40 Hz (Figure 3c), and  $SI$  was under 0.1 (Figure 3d) indicating that the wavefield was dominated by wind sea. From YD 61 to 62, the sea state shifted from wind sea to the mixed-sea conditions and the  $SI$  rapidly shifted from around 0 to 1. After the YD 62,  $SI$  remained fairly constant with a value near unity and  $H_s$  reached its maximum of about 4 m ( $H_s/H_{clim} > 6.8$ ), indicating a YM wave event. The time history of  $f_p$  shows an increasing trend from 0.06 to 0.1 Hz, relating to dispersive wave propagation where faster, longer waves arrive ahead of shorter, slower waves (e.g., Jiang et al., 2016; Munk et al., 1963).

The time series of  $H_s$  during the first half of the YM wave event (YD: 61.8–63.6) exhibited large variability, ranging from 3 to 5 m. At first glance, this is so unusual that one might suspect measurement error. Upon further inspection, we found this to be a consistent signature, commonly observed during YM wave events as seen in Figure S1. We quantify this with the scatter index of  $H_s$  in Table 3. The time series of the sea surface elevation,  $\eta$ , provides a way to further examine characteristics of YM wave phenomena. Figure 3e shows an example of 20-min time series of  $\eta$  with wave envelope  $A$  at YD 62.25 near the peak of the YM wave event.

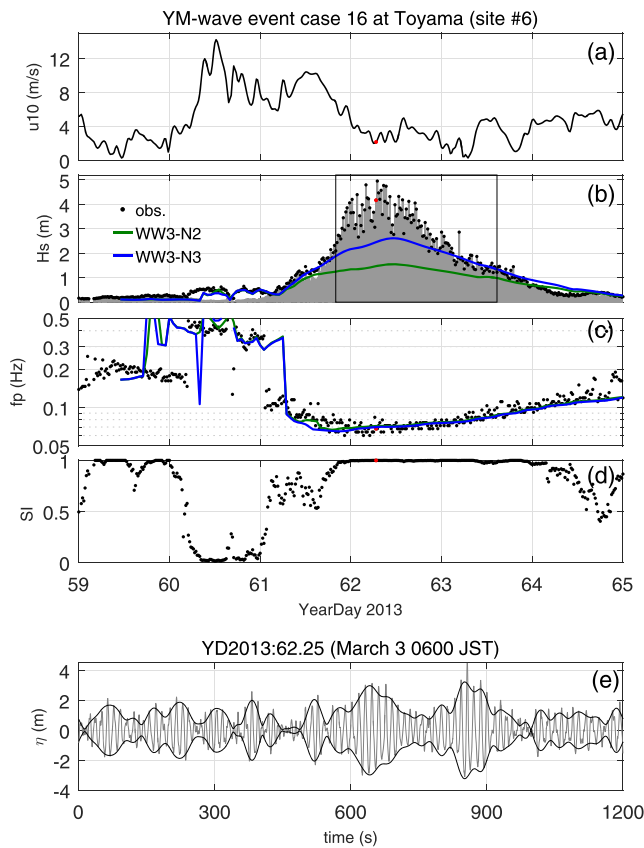


**Figure 3.** Time series of wind and wave statistics during YM wave event case 16 at Toyama site (#6): (a) surface wind speed (m/s) from JMA/MSM products, (b) significant wave height observed by NOWPHAS (black dots) and hindcasted by WW3-N2 model (green line) and WW3-N3 model (blue line). Gray shading represents swell height estimated by  $H_s^{swell} = 4\sqrt{m_s}$  from equation (3). Black box indicates the duration of the YM wave event. (c) Same as (b) but for peak wave frequency; (d) swell index defined in equation (4). (e) An example of the temporal variation of the sea surface elevation (gray thin line) and wave envelope (black line) at YD 62.25 (3 March 2013 0600 JST). The wave envelope is estimated by applying a Hilbert transform to band-passed (from  $0.5f_p$  to  $1.5f_p$ ) sea surface elevation. Red dots in (a)–(d) denote the time of (e).

Wave group structure and modulation of the wave envelope is clearly visible. These are a robust features confirmed in other YM wave events.

To summarize, YM events can be characterized as swell dominated, with wave height larger than the climatological average. They exhibit high variability in the time series of  $H_s$ , and the sea surface elevation exhibit strong wave group structure with modulated wave envelopes. Next, we attempt to explain and reproduce these features of the observations with models.

### 3.2. Swell Propagation Into the TB and Over the Submarine Canyons

In situ point measurements have an inherent limitation: they cannot give insight into how ocean waves evolve over space. Therefore, we examined results from WW3-N2 and WW3-N3 models for their spatially resolved perspective of the YM wave event.

YM wave events typically emanate from the NNE as seen in the ray trajectories in Figure 1a. Hindcasts revealed propagation patterns of swells and the spatial distribution of  $H_s$ . The  $H_s$  is higher in the eastern side of the bay and reduction of  $H_s$  toward the west is a prominent feature (Figure 4a). The swells coming from the open waters (i.e., the Sea of Japan) were partially blocked due to sheltering effect of the Noto Peninsula, which creates shadow zones of relatively lower wave energy over the TB region. Figures 5a and 5b show 2-D wave spectra normalized by their maximum energy at locations TB0 (outside the bay) and TB5 (inner part of the bay) indicated in Figure 4a. Wave energy in the frequency domain was concentrated in the 0.06–0.08 Hz band with spectral peaks at around 0.07 Hz at both locations. The spectra were notably narrow, which was a consequence of dispersive wave propagation.

The most striking difference between 2-D wave spectra inside and outside of the bay was the directional spreading. The wave spectrum at TB0 consisted of two swell systems within  $45^\circ$  emanating from between NE and N, whereas at TB5, there was a single peaked spectrum from the NNE with very narrow spreading. The directional spreading of wave spectra can be quantified by the circular rms spreading  $\sigma_\theta$  proposed by Kuik et al. (1988). This bulk parameter is a standard output for the WW3 and was typically more than  $50^\circ$  for mixed sea (e.g., Tamura et al., 2009, 2010), and around  $10^\circ$  for pure swell conditions (e.g., Ewans, 2002). The lowest value was found at TB5 where  $\sigma_\theta$  was  $7.6^\circ$ .

The transition of the spectral form and the coincident reduction of swell energy are demonstrated in Figure 5d. The directional distributions are shown from TB0 and TB5 plus four additional locations in the middle part of the bay on 37th parallel N (TB1–TB4 in Figure 4a). Directional distributions narrowed from east to west as the northerly spectral components were filtered out by the Noto Peninsula. As a result, the wavefield on the outer shelf in the bay was narrow in both frequency and direction; thus, it could be considered a quasi-monochromatic incident spectrum.

The spatial distribution of  $H_s$  (Figure 4b) shows that the regions with large  $H_s$  appear to correspond with swells encountering submarine canyons. This is due to convergence and divergence of wave energy refracting over the bottom topography. These features were seen in the WW3-N3 model (Figure 4b), and they did not appear in WW3-N2 (Figure 4a) as the continental shelf and submarine canyons were not fully resolved. By serendipity, the NOWPHAS Toyama site was located in one of the wave convergence zones. 2-D wave spectra observed at Toyama (Figure 5c) clearly show bimodal directional distribution ranging from NNW to NNE around the peak frequency of 0.07 Hz.

We compare WW3 results with observation (Figures 3b and 3c). The nested spectral wave models captured the change in  $f_p$  during the YM wave event (Figure 3c) but failed to reproduce the characteristic variability

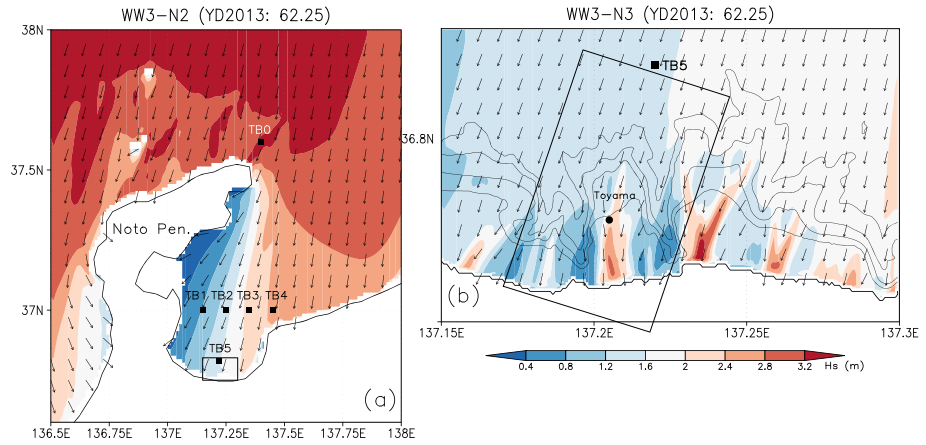


**Figure 4.** (a) Spatial distribution of the significant wave height (colored contours) and peak wave direction (arrows) during the YM wave event at YD 62.25 (year 2913, case 16, see Table 3) hindcasted by WW3-N2. Black squares (from TB0 to TB5) indicate the output locations of wave spectra shown in Figure 5. (b) Same as (a) but hindcasted by WW3-N3 (the innermost domain). The solid rectangle indicates the computational domain for the SWASH model. The black dot represents the observation site Toyama site (#6). The black square (TB5) indicates the output locations of WW3-N2 model used as the incident wave spectra for SWASH computation. The contours of bottom topography (M7000 data set) are also shown at 20, 50, 100, and 200 m. The  $H_s$  fields in (a) is given in the same color in (b).

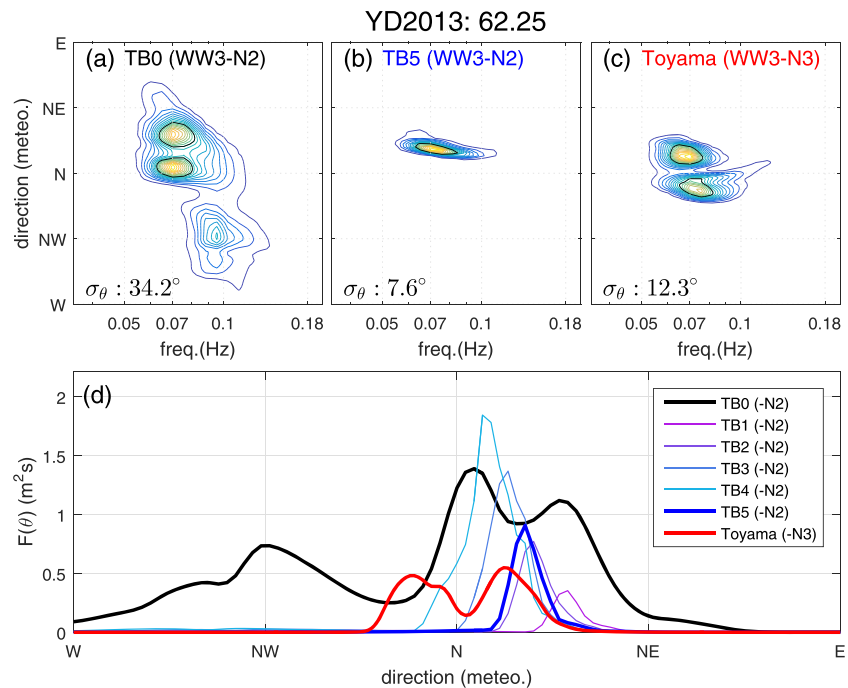


**Figure 5.** Hindcast of 2-D wave spectra at (a) TB0, (b) TB5, and (c) Toyama site (#6) at the same time as shown in Figure 4. The wave spectra are normalized by their maximum values and are shown with the contour interval of 0.05. Black lines represent the energy level of 50% of the maximum values. The values of directional spreading  $\sigma_\theta$  for each 2-D spectra are also indicated. (d) Omnidirectional wave spectra at seven locations (from TB0 to TB5, and Toyama). 2-D and omnidirectional wave spectra were hindcasted by WW3-N2 model for all locations with the exception of Toyama (WW3-N3 model).

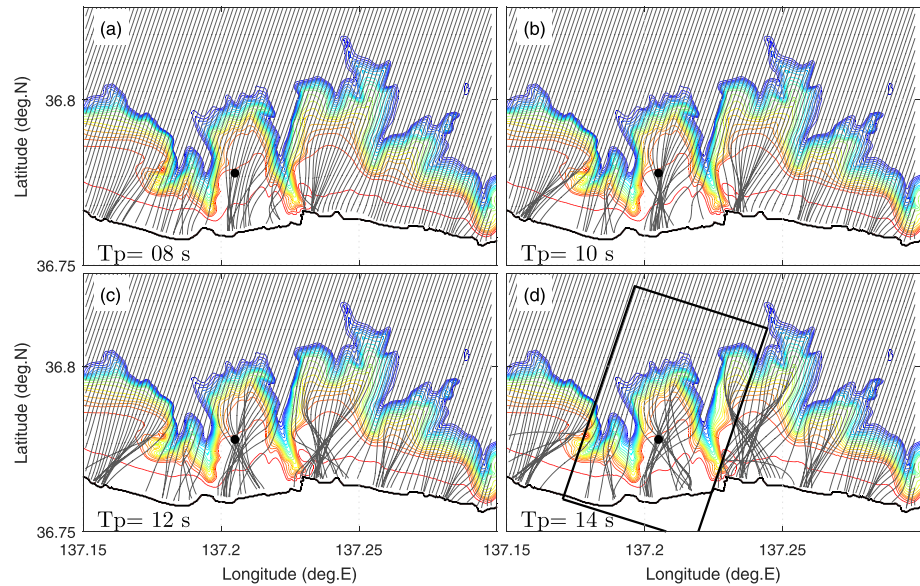


**Figure 6.** Wave ray trajectories for incident wave periods of (a) 8 s, (b) 10 s, (c) 12 s, and (d) 14 s with a fixed incident wave direction from around NNE ( $18^\circ$  clockwise from north), corresponding to an incident wave direction in Figure 5b. Wave rays are imposed from offshore and lateral boundaries. The Toyama observation site is indicated by black dots. The bathymetries from M7000 data set were used for experiments and indicated by colored contours from 0 to 200 m in 10 m intervals. The black rectangle in (d) indicates the SWASH model domain.

of  $H_s$  (Figure 3b). Compared to WW3-N2, the WW3-N3 estimation of  $H_s$  was closer to observations due to the higher resolution, which led to more accurate wave refraction. However,  $H_s$  was significantly underestimated during the first half of the event from YD 61.8 to 63 and with much less variability. The inability to match  $H_s$  variability was a consistent deficiency confirmed in other YM events we investigated (not shown). Further refinement of grids could not completely reproduce the characteristic  $H_s$ . Instead, we hypothesize that the random phase assumption may not hold for YM wave events and a new model is needed.

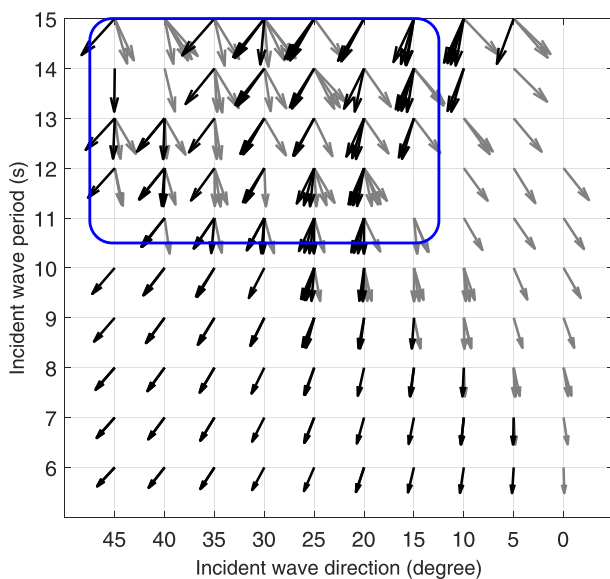


**Figure 7.** The normalized wavenumber vectors for different incident wave conditions at around the Toyama. Black (gray) arrows indicate waves coming from east (west) which are mainly aligned with incident wave direction (veered through refraction). The incident wave angles in the x axis are measured clockwise from north. The blue box highlights the incident wave conditions which induce crossing swell fields at Toyama.

### 3.3. Wave Ray Refraction Over the Continental Shelf

To further explore the mechanisms responsible for the YM wave events, we conducted ray tracing experiments. For this, we extended the ray equation in spherical coordinates by Gallet and Young (2014) to shallow waters. Figure 6 displays ray trajectories for different incident wave periods from 8 to 14 s at a 2-s interval. The wave direction was fixed out of the NNE, which corresponds to the incident wave direction observed in Figure 5b. The wave rays were strongly curved over the steep bottom slope (i.e., submarine canyons), and as the incident wave periods increased, focal zones (or caustics) appeared over the continental shelf. At a period of 14 s (Figure 6d), the spatial pattern of ray density closely corresponds with the spatial pattern of  $H_s$  in Figure 4b; convergence (divergence) zones of wave rays corresponds to higher (lower)  $H_s$  regions. Consequently, the observational site of Toyama is located in a region of ray focusing (crossing sea state) when the incident wave period is larger than about 10 s (Figure 6c).

This is also consistent with the hindcast results from WW3 and the observational evidence. We have seen that, during the YM wave event, the wave spectrum at Toyama site displayed bimodal form in directional distribution with the spectral peak at around 14 s (Figure 5c). In addition, high variability in the wave height over short period of time (i.e., important signature of the YM wave event) was most clearly observed only when the

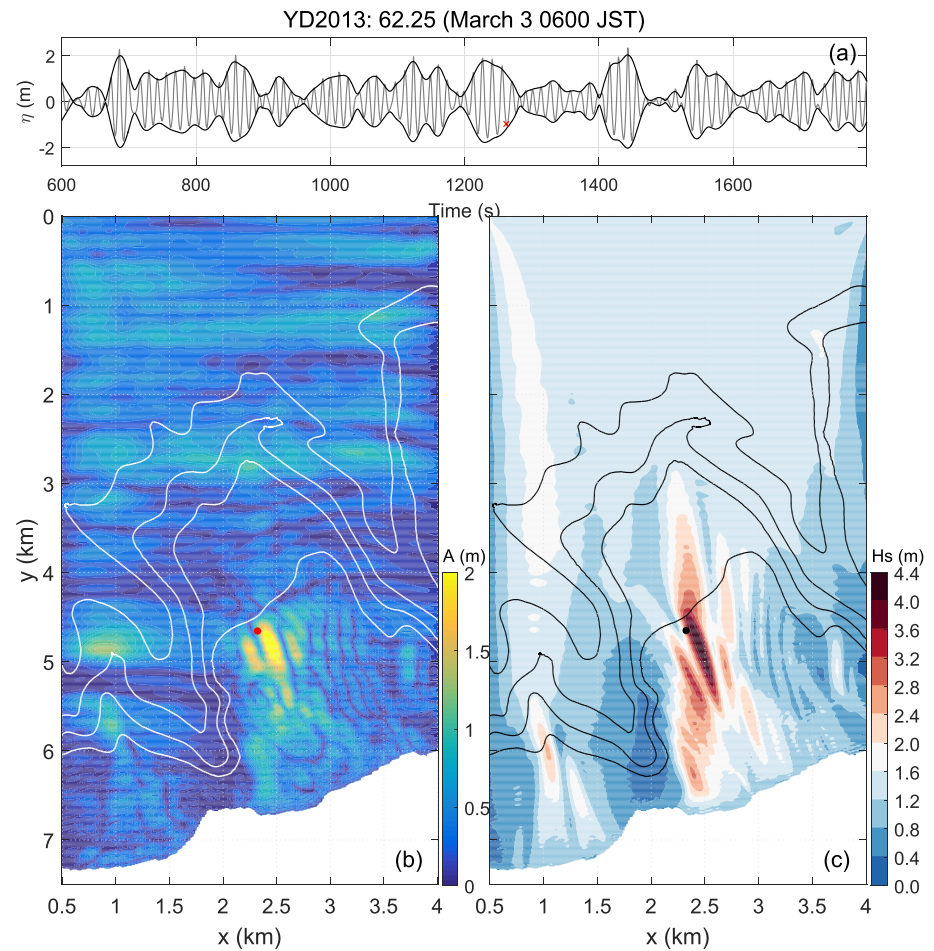


**Figure 8.** SWASH model results of the YM wave event, case 16, at YD 62.25 (JST). (a) Temporal variation of the sea surface elevation and wave envelope at Toyama. (b) The snapshot of wave envelope at the time indicated by the red cross in (a). The red dot presents the Toyama observation site. White contours show bottom topography at 20, 50, 100, and 200 m. (c) The spatial distribution of  $H_s$  calculated from the last 20 min of the sea surface elevation of model run. An animation is available (Movie S1).

peak wave period was larger than around 12 s during the first half of the event (Figures 3b and 3c). From these results, we can speculate that the YM wave event is related to the crossing sea state which is generated by longer swells. Therefore, the incident wave condition is key for generating YM wave events.

This geometric optics approach can be used to test the sensitivity of the ray trajectories to the incident wave conditions. We repeated these experiments, changing the incident wave periods and direction. As we varied the incoming wave properties, we looked at the wave rays at fixed location in the domain (a circle with 50 m radius). In Figure 7, black (gray) arrows indicate waves coming from the east (west), which are aligned with (refracted away from) the incident wave direction. The swell field at Toyama mainly consisted of a combination of easterly and westerly waves. This condition appears to be satisfied by incident wave rays with a period greater than 11 s emanating from northeasterly directions (between  $15^\circ$  and  $45^\circ$ ). Thus, these are the incident wave conditions that lead to YM wave events.

### 3.4. The Formation of YM Waves

So far, observational data, phase-averaged hindcasts, and analytical ray tracing show that for case 16, a nearly monochromatic wave event entered the TB and strongly refracted over the submarine canyons. However, the high variability of  $H_s$  could not be reproduced suggesting that perhaps we are missing some physics due to the violation of our phase-average assumptions. Here, we test the hypothesis that the YM wave events can be explained as the phase-coherent amplification of ocean swells over the submarine canyons. Quasi-monochromatic wave trains are split at the edge of the continental shelf by the steep topography,

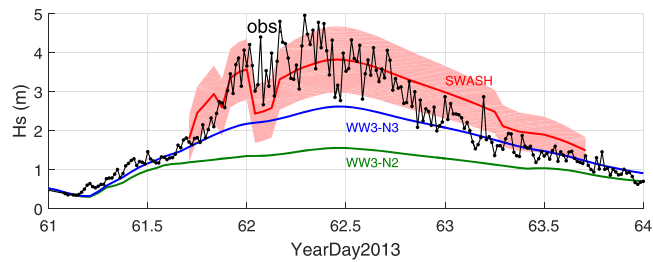


**Figure 9.** Time series of the  $H_s$  hindcasted by SWASH for YM wave event, case 16, in 2013. Temporal variation of  $H_s$  at Toyama is indicated by red line, whereas one standard deviation within a spatial length scale of the interference is shown by red shading. The observation (black line with dots) and WW3-N2 and WW3-N3 hindcasts (green and blue lines, respectively) are also indicated.

then the directionally scattered waves interact with each other over the continental shelf, and thereby the amplitude modulation grows through the coherent interference in focal zones.

Hindcasts of the YM wave event were carried out with SWASH by changing the incident wave spectra on an hourly interval from YD 61.71 to 63.71 (i.e., 2-day hindcast with total of 48 runs) along the offshore boundary ( $y = 0$ ). The hindcast run at YD 62.25 clearly demonstrated characteristic features of swell propagation over the submarine canyons (Figure 8). These results correlated with the observational evidence (Figure 3e) and WW3 model results (Figures 4 and 5). Time series of the sea surface elevation  $\eta$  and wave envelope  $A$  at Toyama are shown in Figure 8a. The wave group structure is apparent in both observations (Figure 3e) and simulations (Figure 8a). The snapshot of the wave envelope in Figure 8b is a typical spatial pattern of swell modulation over the continental shelf. An animation (Movie S1 in the supporting information) shows the

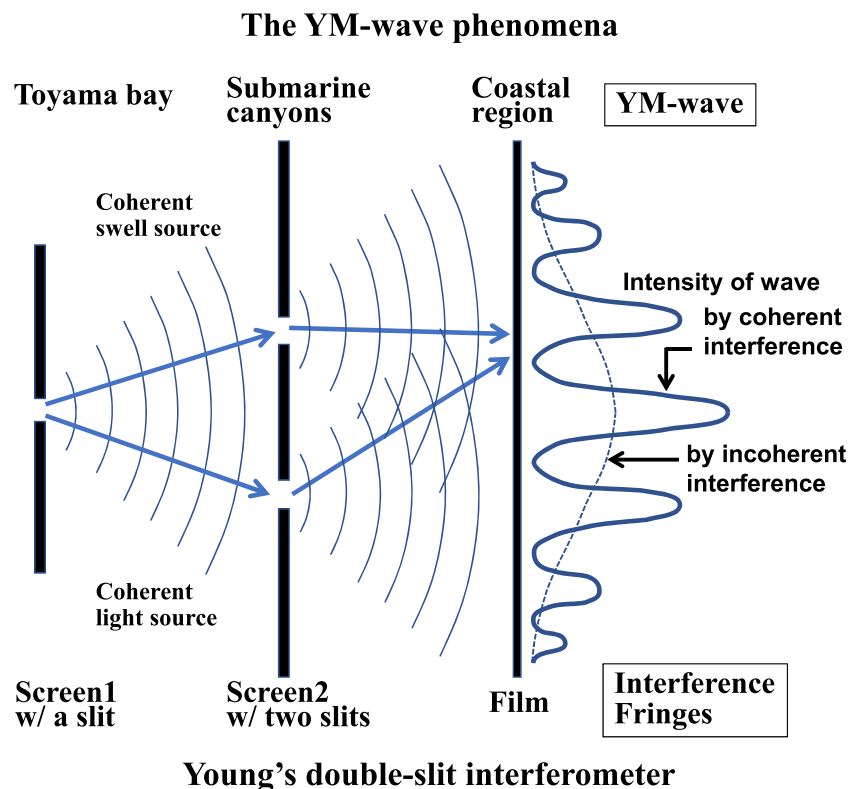


**Figure 10.** Schematic diagram of the YM wave phenomena in relation to the Young's double slit interferometer. The coherent swell (light) source is incident in the Toyama bay (on the first screen with a slit). The continental shelf (second screen) with submarine canyons (two slits) serves as the source of coherent swell (light). The swell (light) waves emerging from the submarine canyons (two slits) interfere and form YM waves (interference fringes) near the coastal region (on the film).

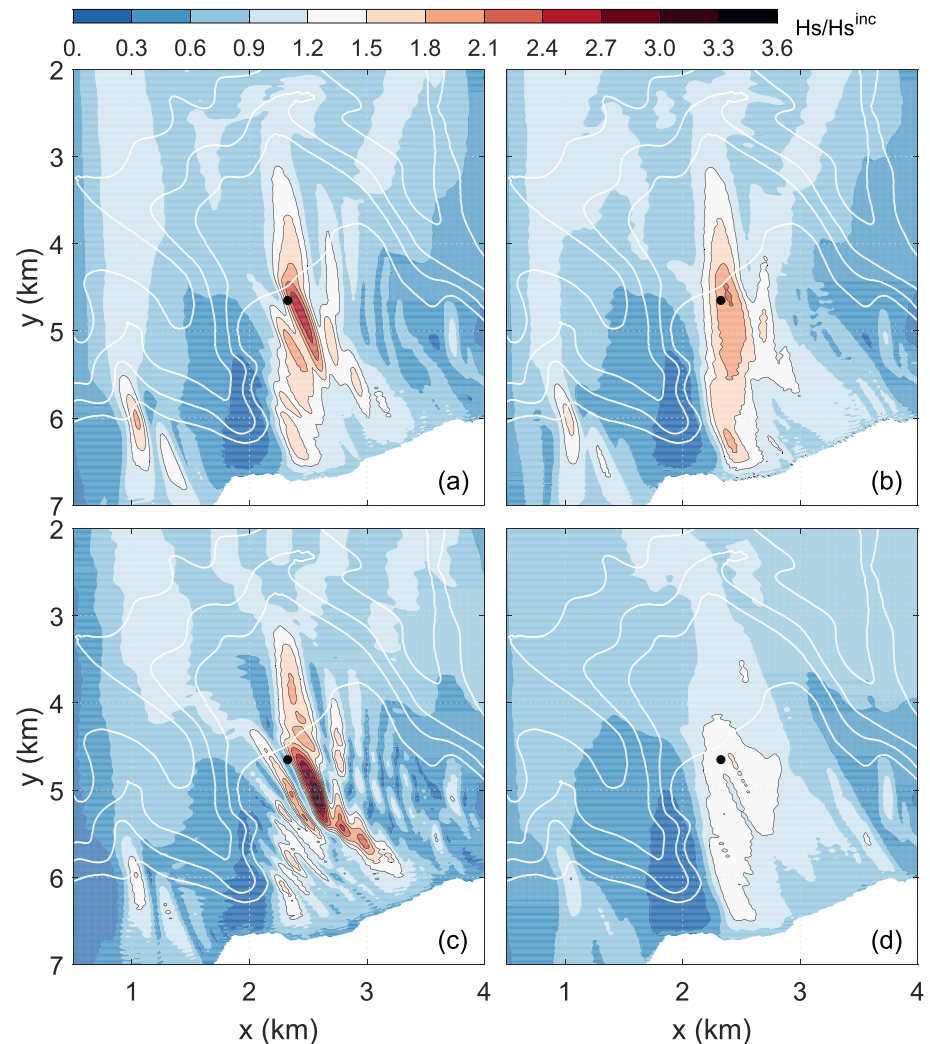


**Figure 11.** Comparison of  $H_s$  fields for different incident wave spectra. The spatial distributions of  $H_s$  are normalized by the incident wave height. (a) Incident wave spectrum hindcasted by WW3-N2 model. (b) same as (a) but hindcasted with relatively lower directional resolution model ( $10^\circ$ ). (c) delta function wave spectrum assuming a monochromatic wave, and (d) broader wave spectrum (the standard JONSWAP spectrum with  $\cos^8 \theta$  angular spreading). Black dots present the Toyama observation site.

evolution of this characteristic pattern more clearly; as the long-crested waves propagate shoreward, spatial oscillations of wave amplitude were enhanced over the continental shelf. The short-crested wave packets were aligned with the wave propagation direction.

The time averaged  $H_s$  field is also shown in Figure 8c, which can be compared with the results from WW3-N3 (Figure 4b). The difference between the deterministic and stochastic models is apparent. The  $H_s$  estimated by the SWASH reached its maximum of about 4+ m which largely exceeds the 2.5 m maxima from WW3. The spatial distribution exhibits small scale features related to persistent constructive/destructive interference (i.e., enhancement and reduction of  $H_s$ ) corresponding to interference fringes seen in Figure 8c. The observation site Toyama is located in the vicinity of the interference fringes where the spatial variation of  $H_s$  is significant.

Time series of  $H_s$  in Figure 9 by the SWASH model (red line) shows a much closer correspondence with the observed  $H_s$ , especially when compared with WW3 model results (green and blue lines). The estimated  $H_s$  values (red line) jump rapidly at around YD 62, 62.16, and 63.29. This is related to a shift of the node-antinode pattern (i.e., interference fringes) in the focal zone according to small changes in the incident wave direction. On the other hand, there was much less variability in the SWASH modeled  $H_s$ . Because incident wave spectra

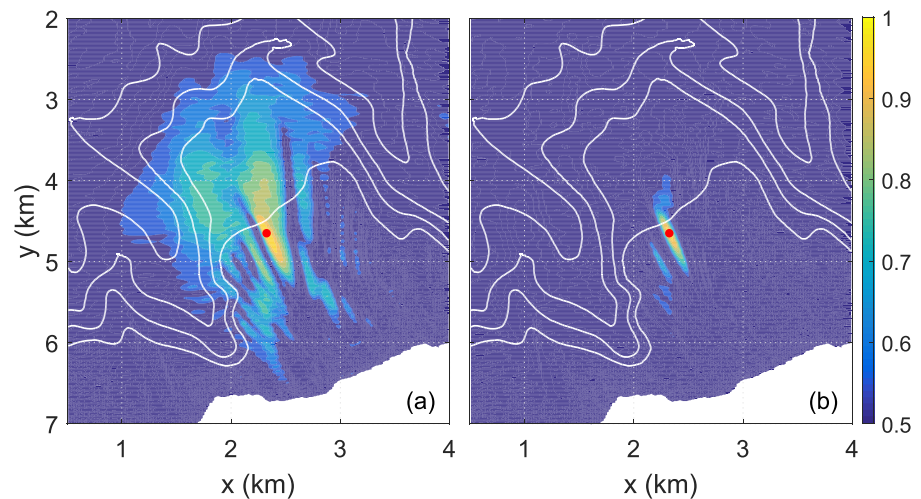


**Figure 12.** (a) Spatial distribution of the lead/lag correlation coefficients of wave envelope at Toyama (red dot) with those at different grid points for the  $H_s$  field of Figure 11a. (b) Same as (a) but for Figure 11b. White contours show bottom topography at 20, 50, 100, and 200 m.

estimated by the WW3 represent some kind of ensemble averaged field, it was unable to reproduce the short term variability of  $H_s$  in the models (i.e., both the WW3 and the SWASH).

Also shown is the range of  $H_s$  variability in space (red shadings in Figure 9). The spatial variation of  $H_s$  in cross wave ( $x$ ) direction is apparent in Figure 8c. A spatial scale related to coherent interference,  $\lambda$ , can be calculated according to Smit et al. (2016), where  $\lambda = 2\pi|\Delta k_{12}^x|^{-1}$  and  $\Delta k_{12}^x$  is the wavenumber difference of two primary wave components (i.e.,  $N = 2$  in equation (1)). The red shadings represent the one standard deviation of  $H_s$  in spatial domain of  $\lambda$ , and the observations lie within this range. This result demonstrates the possibility to reproduce the unique characteristics of YM wave events with SWASH.

#### 4. Discussion

We would like to point out that YM wave phenomena can also be interpreted in analogy to Young's double-slit interference experiment (Figure 10). Young (1807) demonstrated that two waves originating from a coherent light source interfere and produce dark and bright bands (interference fringes) on a film. If a light source is white (a wide spectrum source), the resulting interference pattern does not appear. In our case, a quasi-monochromatic wave source is achieved by the dispersive wave propagation in frequency domain and by the sheltering effect of the Noto Peninsula in the directional domain. The initially single peaked swell spectrum results in two coherent swells peaks that refract over the submarine canyons and creates interference fringes similar to the double-slit interferometer.

Therefore, interference fringes manifest with characteristics that depend on the incident wave source. Laboratory observations in a similar situation demonstrated that the directional spreading of the incident wave had substantial effect on the wavefield over a submerged shoal (Vincent & Briggs, 1989). Smit and Janssen (2013) also showed that the coherent interference is sensitive to the directional spreading of the incident wave. We expect similar sensitivity of our case of the YM wave event. We performed additional numerical experiments by SWASH with fixed  $H_s$ ,  $f_p$ , and peak wave direction but variable spectral peakedness and directional spreading. We compared four cases: (a) was forced by WW3-N2 (same as previous hindcasts), (b) used WW3-N2 with reduced directional resolution ( $10^\circ$ ), (c) was a monochromatic case, and (d) was a standard JONSWAP spectrum (Hasselmann et al., 1973) with  $\cos^8\theta$  angular spreading function.

Figure 11 shows the  $H_s$  distribution normalized by the incident wave height ( $H_s^{inc}$ ) for the different incident spectra. The pattern of interference fringes of  $H_s$  varied in response to the incident spectral shapes. As expected, small scale variability in the spatial distribution of  $H_s$  was most pronounced when the incident wavefield was monochromatic (Figure 11c). For this case,  $H_s$  amplification reached 3.5 times the incident wave height. On the other hand, when the incident wave spectrum was more broad (Figure 11d), the interference fringes were smoothed out, and the  $H_s$  was only 1.5 times the incident wave height. In Figure 11b,

the incident wave spectrum was supplied by a modified version of WW3-N2 with coarser directional resolution of  $10^\circ$ . This is the resolution of a typical operational wave model. Comparing to Figure 11a, the amplification of  $H_s$  and the node-antinode structure of the interference fringes are significantly weakened.

Figure 12 depicts the spatial distribution of the lead/lag correlations of wave envelopes at Toyama with those at different grid points in SWASH. The envelope signals for each location are led or lagged in time so as to obtain the maximum correlation coefficients. For the  $H_s$  fields where the interference fringes are apparent (Figure 11a), the high positive correlation area extends to up- and down-wave regions over the continental shelf, whereas the correlation coefficient decays very quickly in relation to nodal lines (Figure 11a). This result clearly demonstrates that the wavefield over the canyons is coherent when the directional spreading is narrow. On the other hand, for the  $H_s$  fields where the interference fringes are obscured (Figure 11b), the high positive correlation area is mainly confined to the vicinity of Toyama as a result of the incoherent interference (Figure 11b).

## 5. Conclusions

We have investigated high-energy, swell-dominated wave events in TB, the so-called YoriMawari-nami, to better understand their generation mechanisms, unique features, and predictability. To this end, we analyzed NOWPHAS wave observations, performed wave hindcasts with phase-averaged models, performed hindcast and sensitivity tests with a phase-resolving model, and employed analytical ray tracing techniques. For a particular YM wave event, which was an archetype YM event (case 16), we have shown that incident waves were quasi-monochromatic. Consequently, the swell refracted over the submarine canyon resulting in directional spectra with bimodal directional distribution emanating from two different directions. This initiated conditions favorable for coherent interference violating the assumptions of the phase-averaged approach, which explains why engineers have struggled to reproduce these events with phase-average models (e.g., WW3). SWASH, a phase-resolving model, was used to test the hypothesis that an important part of the formation of YM wave events is phase-coherent interference that generates strong modulation of wave amplitude. We demonstrated that interference fringes were generated over the submarine canyon, and only through the phase-resolving model were we able to adequately reproduce the observed mean and variability of  $H_s$ .

## Acknowledgments

We are grateful to Lie-Yauw Oey (Princeton University) and an anonymous reviewer for their careful reading of the paper and their constructive comments, which were very helpful in improving the manuscript. H. T. acknowledges discussions with Tomohiro Suzuki (Flanders Hydraulics Research), Clarence O. Collins III (U.S. Army Engineering Research and Development Center), and Mitsuhiro Tanaka (Gifu University) during the preparation of this manuscript. This work was partly supported by JSPS KAKENHI Grants JP16H04423 and JP17H03317. The NOWPHAS data set (available online at [https://www.mlit.go.jp/kowan/nowphas/index\\_eng.html](https://www.mlit.go.jp/kowan/nowphas/index_eng.html)) was provided by the Ministry of Land, Infrastructure, Transport and Tourism in Japan. The JMA operational atmospheric products are available online (at <http://database.rish.kyoto-u.ac.jp/arch/jmadatadata/gpv/>).

## References

- Ardhuin, F., Chapron, B., & Collard, F. (2009). Observation of swell dissipation across oceans. *Geophysical Research Letters*, *36*, L06607. <https://doi.org/10.1029/2008GL037030>
- Badulin, S. I., & Zakharov, V. E. (2017). Ocean swell within the kinetic equation for water waves. *Nonlinear Processes in Geophysics*, *24*(2), 237–253.
- Battjes, J. A., & Janssen, J. P. F. M. (1978). Energy loss and set-up due to breaking of random waves. In *Proceedings of 16th Conference on Coastal Engineering*, Hamburg, Germany, pp. 569–587.
- Bidlot, J. R., Janssen, P. A. E. M., & Abdalla, S. (2007). A revised formulation of ocean wave dissipation and its model impact. ECMWF Technical Memoranda 509.
- Cavaleri, L., Alves, J.-H. G. M., Ardhuin, F., Babanin, A., Banner, M., Belibassakis, K., et al. (2007). Wave modelling—The state of the art. *Progress in Oceanography*, *75*(4), 603–674.
- Didenkulova, I., Pelinovsky, E., & Soomere, T. (2009). Long surface wave dynamics along a convex bottom. *Journal of Geophysical Research*, *114*, C07006. <https://doi.org/10.1029/2008JC005027>
- Donelan, M. A., Hamilton, J., & Hui, W. H. (1985). Directional spectra of wind-generated ocean waves. *Philosophical Transactions of the Royal Society of London. Series A*, *315*(1534), 509–562.
- Ewans, K. C. (2002). Directional spreading in ocean swell. In *Fourth International Symposium on Ocean Wave Measurement and Analysis*, San Francisco, California, United States.
- Gallet, B., & Young, W. R. (2014). Refraction of swell by surface currents. *Journal of Marine Research*, *72*(2), 105–126.
- Hasselmann, K., Barnett, T. P., & Bouws, E. (1973). Measurements of wind-wave growth and swell decay during the Joint North Sea Wave Project (JONSWAP). *Deutsche hydrographische Zeitschrift: Ergänzungshefte /A*.
- Hasselmann, S., Hasselmann, K., Allender, J. H., & Barnett, T. P. (1985). Computations and parameterizations of the nonlinear energy transfer in a gravity-wave spectrum. Part II: Parameterizations of the nonlinear energy transfer for application in wave models. *Journal of Physical Oceanography*, *15*(11), 1378–1391.
- Jiang, H., Babanin, A. V., & Chen, G. (2016). Event-based validation of swell arrival time. *Journal of Physical Oceanography*, *46*(12), 3563–3569.
- Kats, A. V., & Kontorovich, V. M. (1971). Drift stationary solutions in the weak turbulence theory. *JETP Letters*, *14*, 265–267.
- Kohno, N., Ichikawa, H., Tauchi, T., & Kanai, Y. (2009). The mechanism of the high wave YoriMawari-Nami on 24th February 2008. Proc. 11th Int. Workshop on Wave Hindcasting and Forecasting.
- Kuik, A. J., van Vledder, G. Ph., & Holthuijsen, L. H. (1988). A method for the routine analysis of pitch-and-roll buoy wave data. *Journal of Physical Oceanography*, *18*(7), 1020–1034.
- Magne, R., Belibassakis, K. A., Herbers, T. H. C., Ardhuin, F., O'Reilly, W. C., & Rey, V. (2007). Evolution of surface gravity waves over a submarine canyon. *Journal of Geophysical Research: Oceans*, *112*, C01002. <https://doi.org/10.1029/2005JC003035>

- Munk, W. H., Miller, G. R., Snodgrass, F. E., & Barber, N. F. (1963). Directional recording of swell from distant storms. *Philosophical Transactions of the Royal Society of London. Series A, Mathematical and Physical Sciences*, 255(1062), 505–584.
- Ohta, T., Matsuura, T., Murakami, T., & Shimokawa, S. (2016). Wave characteristics of Yori-Mawari wave caused by topographic effects. *Journal of Japan Society of Civil Engineers, Ser. B3 (Ocean Engineering)*, 72(2), I\_289–I\_294.
- Smit, P. B., Bland, R., Janssen, T. T., & Laughlin, B. (2016). Remote sensing of nearshore wave interference. *Journal of Geophysical Research: Oceans*, 121, 3409–3421. <https://doi.org/10.1002/2016JC011705>
- Smit, P. B., & Janssen, T. T. (2013). The evolution of inhomogeneous wave statistics through a variable medium. *Journal of Physical Oceanography*, 43(8), 1741–1758.
- Smit, P. B., Janssen, T. T., & Herbers, T. H. C. (2015). Stochastic modeling of coherent wave fields over variable depth. *Journal of Physical Oceanography*, 45(4), 1139–1154.
- Smit, P. B., Janssen, T. T., Holthuijsen, L., & Smith, J. (2014). Non-hydrostatic modeling of surf zone wave dynamics. *Coastal Engineering*, 83, 36–48.
- Snodgrass, F. E., Hasselmann, K. F., Miller, G. R., Munk, W. H., & Powers, W. H. (1966). Propagation of ocean swell across the Pacific. *Philosophical Transactions of the Royal Society of London. Series A, Mathematical and Physical Sciences*, 259(1103), 431–497.
- Suzuki, T., Altomare, C., Veale, W., Verwaest, T., Trouw, K., Troch, P., & Zijlema, M. (2017). Efficient and robust wave overtopping estimation for impermeable coastal structures in shallow foreshores using swash. *Coastal Engineering*, 122, 108–123.
- Tamura, H., Waseda, T., & Miyazawa, Y. (2009). Freakish sea state and swell-windsea coupling: Numerical study of the Suwa-Marui incident. *Geophysical Research Letters*, 36, L01607. <https://doi.org/10.1029/2008GL036280>
- Tamura, H., Waseda, T., & Miyazawa, Y. (2010). Impact of nonlinear energy transfer on the wave field in Pacific hindcast experiments. *Journal of Geophysical Research*, 115, C12036. <https://doi.org/10.1029/2009JC006014>
- Tolman, H. L. (2009). User manual and system documentation of WAVEWATCH III TM version 3.14. National Centers for Environmental Prediction, National Weather Service, NOAA, Camp Springs, Md.
- Tsuboki, K., & Wakahama, G. (1992). Mesoscale cyclogenesis in winter monsoon air streams: Quasi-geostrophic baroclinic instability as a mechanism of the cyclogenesis off the west coast of Hokkaido Island, Japan. *Journal of the Meteorological Society of Japan. Series II*, 70(1), 77–93.
- Vincent, C. L., & Briggs, M. J. (1989). Refraction-diffraction of irregular waves over a mound. *Journal of Waterway, Port, Coastal, and Ocean Engineering*, 115(2), 269–284.
- Yanase, W., Niino, H., Watanabe, S. I., Hodges, K., Zahn, M., Spengler, T., & Gurvich, I. A. (2016). Climatology of polar lows over the sea of Japan using the JRA-55 reanalysis. *Journal of Climate*, 29(2), 419–437.
- Young, T. (1807). *A course of lectures on natural philosophy and the mechanical arts* (Vol. 1). London: Printed for J. Johnson.
- Young, I. R. (2006). Directional spectra of hurricane wind waves. *Journal of Geophysical Research*, 111, C08020. <https://doi.org/10.1029/2006JC003540>
- Young, I. R., & Van Vledder, G. P. (1993). A review of the central role of nonlinear interactions in wind-wave evolution. *Philosophical Transactions of the Royal Society of London. Series A: Physical and Engineering Sciences*, 342(1666), 505–524.
- Zakharov, V. (2018). Analytic theory of a wind-driven sea. *Procedia IUTAM*, 26, 43–58.
- Zakharov, V. E., Badulin, S. I., Geogjaev, V. V., & Pushkarev, A. N. (2019). Weak-turbulent theory of wind-driven sea. *Earth and Space Science*, 6(4), 540–556.
- Zijlema, M., Stelling, G., & Smit, P. (2011). Swash: An operational public domain code for simulating wave fields and rapidly varied flows in coastal waters. *Coastal Engineering*, 58(10), 992–1012.